Forearc Stresses in the Northern Cascadia Subduction Zone

A Thesis Submitted to the faculty of the University of Minnesota by

Joseph Rippke

In partial fulfillment of the requirements for the degree of
Master of Science

Advisor: Ikuko Wada

August 2020

Acknowledgements

I would like to thank the Earth Science department, my academic home since 2014, for supporting me and nurturing my academic growth. The administrators, faculty, and staff of the department have been there for me time and time again. I would especially like to thank my advisor, Ikuko Wada, for her unwavering support, guidance, and patience over the years.

I would also like to thank Katsumi Matsumoto for advising my undergraduate research, exposing me to numerical modeling, and guiding me through my first research experiences.

I would like to thank the people of the Wada lab: Lindsay Kenyon, Like An, Trey Brink, Xin Zhou, and Kingsley Anyim. Learning and working beside you has been a joy.

Finally, I would like to thank my wife, Ashleigh, for her loving support through all of the challenges and successes of my academic journey.

Abstract

We investigate the spatial variation in the state of stress in the overriding plate in the forearc region of northern Cascadia. The key forces that act on the forearc region are the plate coupling force, the northward push of the Oregon block, the gravitational collapse force on elevated topography, and buoyancy of the serpentinized mantle wedge. The latter two forces are expected to cause margin-normal tension at shallow depths in the inner forearc. In this study, we compile available earthquake focal mechanism solutions and determine spatial variations of stress orientation through focal mechanism inversion. The results indicate the maximum compressive stress axis is margin-normal in the outer forearc due to shear stress at the subduction interface and margin-parallel throughout the inner forearc with varying orientations of the intermediate and minimum compressive stress axes throughout the inner forearc, consistent with previous studies. Using a 3-D finite-element code for lithospheric deformation, we explore the effects of gravitational collapse force, the buoyancy of the serpentinized mantle wedge corner, the plate coupling force, the shape of the slab, and the Oregon push on the stress field. The results indicate the buoyancy of the serpentinized mantle wedge corner and the shape of the slab may be as important of contributors to the the state of stress in the inner forearc as the plate coupling force whereas the gravitational collapse force and the Oregon push have a minimal effect on the state of stress in the inner forearc.

Table of Contents

List of Tables

List of Figures

1. Introduction

In subduction zones, tectonic plates undergo significant permanent deformation, producing earthquakes both in the overriding and subducting plates. Earthquakes in the subducting plate are never as large as the largest earthquakes that occur along the subduction faults but can cause significant damage when they occur at relatively shallow depths (e.g., 2001 Mw6.8 Nisqually earthquake in Washington and 2001 Mw 6.7 Geiyo earthquake in Southwest Japan). Earthquakes in the overriding plate are generally even smaller in size but can also be damaging given their proximity to the surface. Earthquakes occur due to tectonic stresses, and understanding their orientations and magnitudes and the forces that induce these stresses is critical to the studies of plate deformation, earthquake generation, and hazard mitigation.

The state of stress in the forearc region of the overriding plate depends strongly on the strength of mechanical coupling between the plates (plate coupling force), which causes horizontal compression (**Figure 1**). The direction of compression relative to the margin depends on the direction of place convergence. Plate convergence oblique to the margin can result in margin-parallel compression (Wang, 1996). The state of stress also depends on the margin topography; sloped topography results in gravitational collapse, which causes horizontal tension (Wang and He, 1999). Presence of other tectonic boundary forces and lateral density variation also affect the state of stress.

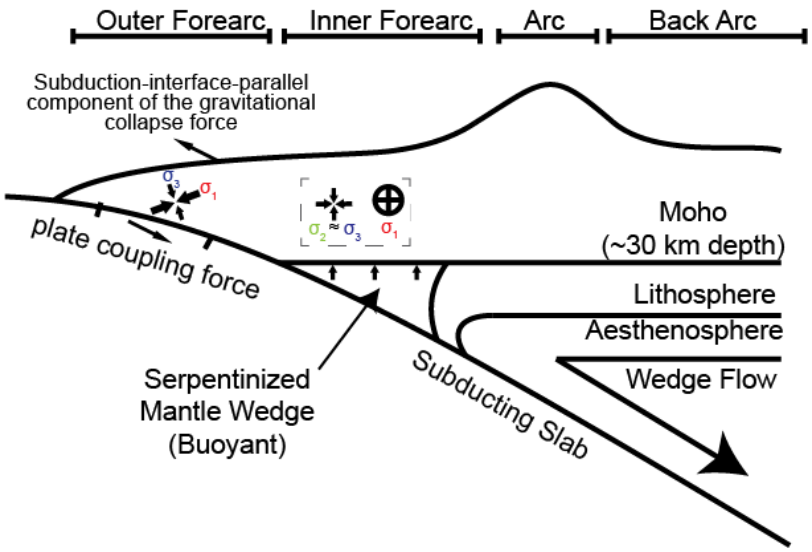

Figure 1. Schematic diagram showing forces acting on the overriding crust in northern Cascadia, namely the plate coupling force, Oregon push, gravitational collapse force on elevated topography, and buoyant force of the serpentinized mantle wedge. The latter two forces are expected to cause margin-normal tension at shallow depths. The state of stress in the outer and inner forearcs that are constrained by previous work (e.g., Wang and He, 1999; Balfour et al., 2011) and this study are indicated using arrows. Circle with a cross inside indicates that σ_1 is parallel to the margin. The combined effect of the gravitational collapse force and buoyancy of the serpentinized mantle wedge must be similar in magnitude to the plate coupling force to cause $\sigma_2 \approx \sigma_3$ in the inner forearc.

In the outer part of the forearc close to the trench, margin-normal horizontal compression is commonly observed through the occurrence of thrust faulting, indicating the plate coupling force as the predominant force (**Figure 1**). However, in the inner part of the forearc closer to the arc, the state of stress is not always or everywhere margin-normal compression, such as in northern Cascadia (Balfour et al., 2011) and NE Japan (Yoshida et al., 2015), indicating the effects of forces other than plate coupling. Further, detailed stress analyses at these subduction zones indicate spatial variations in the stress orientations

within a given forearc system. The causes of such variations have not been quantitatively studied.

In this study, we focus on the northern Cascadia forearc, which is home to three major urban areas of population greater than 2.4 million people: Portland, Seattle, and Vancouver (**Figure 2**). Hazards associated with subduction (seismicity and volcanism) in close proximity to population centers highlight the importance of understanding the dynamics of the Cascadia forearc. Catalogs of focal mechanism solutions and continuous Global Positioning System (GPS) observations throughout Cascadia provide deformational and geodetic data that are critical to studying the forearc stresses. Unlike in the southern portion of Cascadia, the slab forms a concave-downward structure under the arc in northern Cascadia, and the dip direction and angle of the subducting slab varies along the margin. Furthermore, the subduction obliquity transitions from ~40° in the southern half, to ~0° in the northern portion, and it is likely to generate a unique stress field. Margin-parallel compression has been reported in the forearc region of several subduction zones and has been attributed to oblique subduction and other local tectonic forces, such as the northward push of the Oregon block (hereafter referred to as the Oregon push) (Wang, 1996; McCaffrey et. al., 2007).

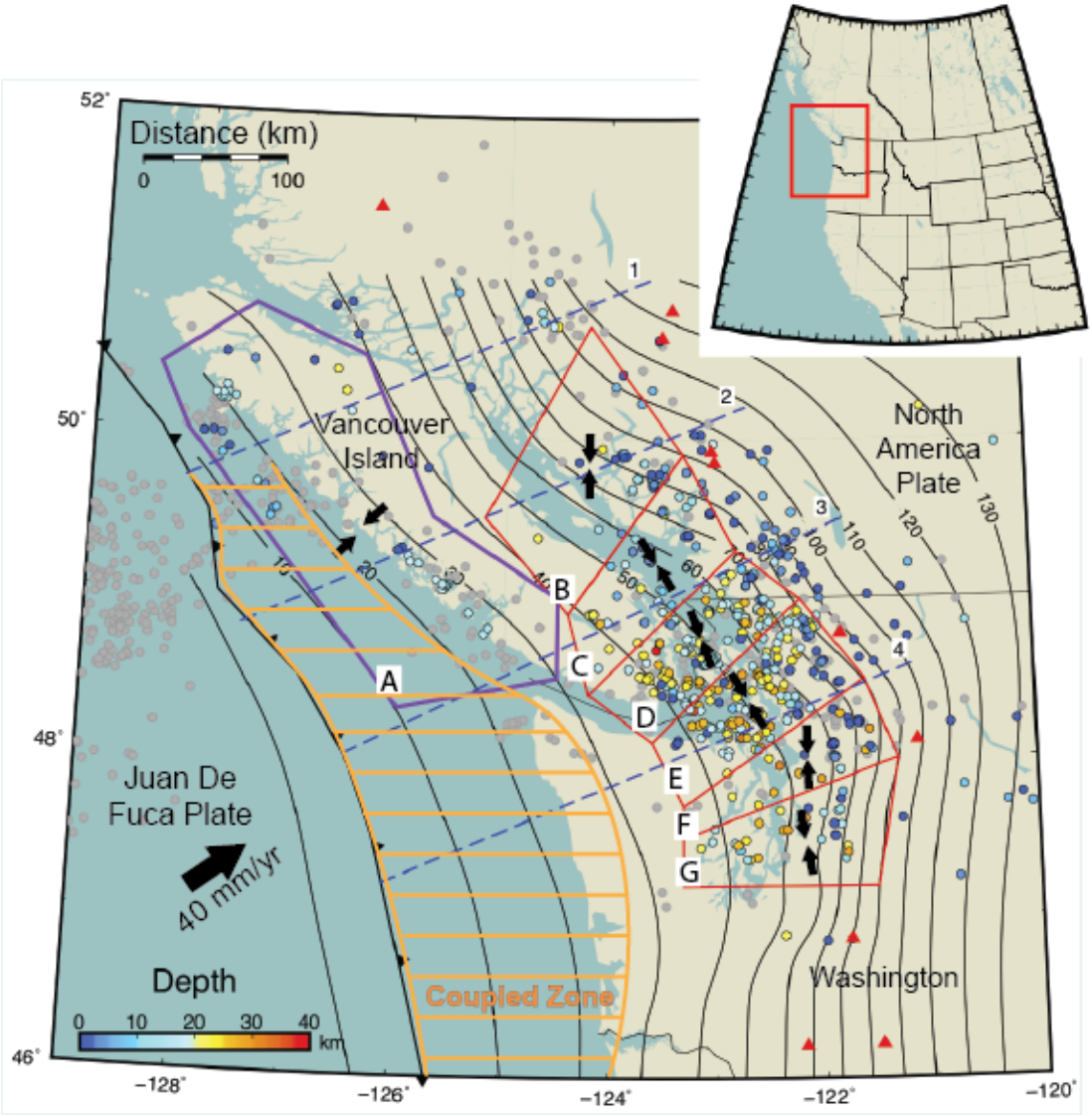

Figure 2. Tectonic setting of the northern Cascadia subduction zone. Circles indicate earthquake locations that are compiled in this study; gray circles are excluded from this analysis, otherwise the color indicates the depth. Red and purple polygons indicate inner and outer forearc sub-regions that are selected for focal mechanism inversion. Blue dashed lines indicate locations of the vertical cross-sections shown in **Figure 3**. Red triangles indicate arc volcanoes. Thin lines indicate slab surface depths contours (km) (McCrory et al., 2006). The orange cross hatched area is the frictionally coupled zone, corresponding to the area between the trench and the downdip extent of the seismogenic zone (Boyarko et al., 2015).

The stress and strain orientations that are constrained by seismic and geodetic data are generally consistent with the Oregon push, but the stress magnitude remains poorly defined. Further, the mantle wedge corner beneath the forearc is reported to be hydrated by slab-derived fluids, forming serpentinites that are less dense than the surrounding mantle (Ramachandran et al, 2006). Together with the plate coupling force and gravitational collapse force, the upward force exerted by the buoyant serpentinized mantle wedge likely generates lateral variation in the state of stress in the overriding crust. In this study we first determine the orientation of the principal stresses in the Cascadia forearc by inverting earthquake focal mechanisms in selected sub-regions where data are available. We build upon the dataset of focal mechanisms compiled by Balfour et. al. (2011) and invert using the linear inversion scheme of Michael (1984).

We model the stress field of simplified and quasi-static forearc systems to quantify the stresses that are induced by (1) the buoyancy of the serpentinized mantle wedge corner by including a buoyant serpentinized zone in our model domains, (2) the northward push of the Oregon block by imposing a realistic displacement on the “south” edge of the model, (3) the plate coupling force, and (4) gravitational collapse force. The basal shear by the subducting Juan de Fuca plate that is expected to cause margin-parallel compression is the margin-parallel component of the plate coupling force. In this study, however, we focus on the role of the margin-normal component of the basal shear in generating margin-normal variation in the state of stress in the forearc.

2. Stress Orientations in the Inner Forearc

2.1. Data: Earthquake Focal Mechanism Solutions

Balfour et al. (2011) compiled 939 first-motion solutions. Of those, 550 solutions for the 2002–2009 period were determined by Balfour et al. (2011), 278 solutions for the 1992–2001 period were reported by the Canadian National Seismic Network (CNSN), and 111 solutions for the 1975-1991 period are from Mulder (1995). Balfour et al. (2011) rated the quality of these solutions from 1 to 5 where 1 is the highest quality and 5 is the lowest quality. We exclude solutions of quality 5, and after removing four duplicates, 678 solutions remain.

In this study, we include centroid moment tensor solutions determined by Natural Resources Canada (NRCan) for events that occurred in a region between longitudes -129 and -120 and latitudes 47N and 52N during January 1, 2000 – September 13, 2019 [Kao et al., 2012; H. Kao, personal communication]. The solutions are rated (1) A–F based on the inversion misfit and (2) 1–4 based on compensated linear vector dipole (CLVD) components where A and 1 are the highest quality for the two criteria (Kao et al., 2012). We exclude one solution for being quality F. After removing duplicates, 277 solutions remain. Of those, only 12 solutions are located in the overriding plate.

We also include moment tensor solutions determined by the USGS for events in the same spatial and temporal region as the CMT solutions from NRCan. The USGS moment tensor solutions were not published with an

assigned quality rating. After removing duplicates, 18 solutions remain. Of those, only 7 solutions are located in the overriding plate. The USGS also published 21 first motion solutions that meet our search criteria. However, all 21 first motion solutions are duplicates and are excluded from this study.

For duplicate solutions in the compilation, solutions from the Balfour (2011) dataset are selected over solutions from the other datasets, followed by the NRCan centroid moment tensor solutions, USGS moment tensor, and USGS first motion datasets. After removing duplicates, 973 solutions remain. The uncertainty in hypocentral depth is expected to be relatively large for offshore events due to sparse seismic networks. To ensure that our data set does not include events in the subducting slab or along the subduction interface, we exclude 354 events that are within a 2.5 km vertical distance from the slab surface and deeper based on the slab surface geometry model of McCrory et al. (2006), leaving 619 solutions in total for analysis (**Figures 2** and **3**).

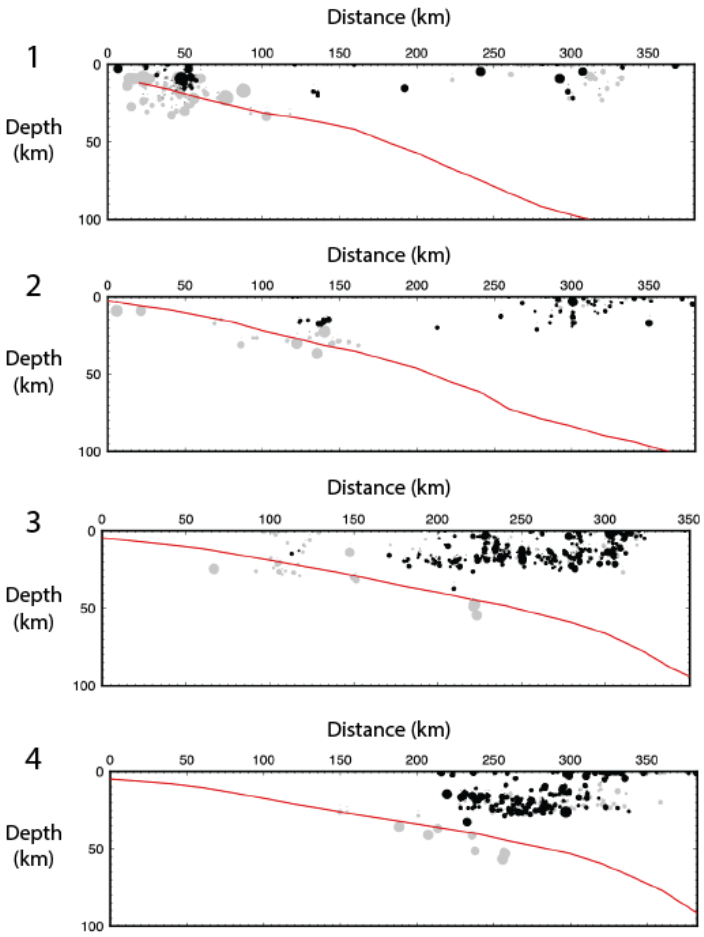

Figure 3. Vertical cross sections through the forearc of northern Cascadia, showing the distribution of earthquakes that are used in the stress analyses in the present study (black circles) and those that are excluded from the analyses (gray circles). The red line represents the surface of the subducting slab (McCrory et al., 2006). The diameter of circles is proportional to the earthquake magnitude. The cross section locations are shown in **Figure 2**.

2.2. Method: Focal Mechanism Inversion

We constrain the orientations of the maximum, intermediate, and minimum (compressive) principal stresses (σ_1, σ_2, and σ_3, respectively) by using the linear earthquake focal mechanism inversion algorithm of Michael (1984, 1987). Many inversion methods exist (e.g., grid search, bayesian), and all are based on the

concept that σ_1 and σ_3 lie within the compressional and tensional quadrants of a focal mechanism, respectively. Variety in focal mechanisms is required to constrain the principal stress orientations within these quadrants; inverting the focal mechanisms of the same type is equivalent to inverting a single focal mechanism. Such a requirement can be satisfied if earthquakes occur on faults with differing orientations. Focal mechanism inversion is based on the assumption that the focal mechanisms describe the deformation under a uniform stress field, requiring some knowledge of regional tectonics to select the area for which the inversion is to be applied.

The focal mechanism inversion does not allow the determination of the magnitudes of the principal stresses but provides their relative magnitudes expressed in terms of ϕ:

$$\phi = \frac{\sigma_2 - \sigma_3}{\sigma_1 - \sigma_3} \tag{1}$$

The value of ϕ ranges from 0 to 1. Values close to zero indicate that the magnitudes of σ_2 and σ_3 are similar, and values close to one indicate that the magnitudes of σ_1 and σ_2 are similar.

The uncertainties in the principal stress orientations are expressed in terms of 95% bootstrap confidence intervals (Michael 1987), and we use 2000 resamplings. Larger confidence intervals (regions) indicate greater uncertainties, and where the intervals of principal stresses overlap for a given inversion, their orientations are poorly resolved.

We select seven sub-regions in the forearc based largely on earthquake distribution and the geometries of the forearc and the subducting slab (**Figure 2**) and perform focal mechanism inversion for each sub-region. One sub-region (A) is in the outer forearc, and the other six are in the inner forearc (B–G). We choose inner forearc regions to border the volcanic arc, roughly following the 80-90 km depth contour lines of the slab. The trenchward border of the inner forearc sub-regions roughly follows the 30-40 km depth contours of the slab along the middle of the forearc. We divide this region with margin-normal boundaries that are closer together in areas of dense earthquake distribution. Whether the assumption of uniform stress state within each sub-region is valid is discussed in **Section 2.3**. We also treat Sub-regions D–F, where there are relatively large numbers of focal mechanism solutions, as one sub-region and divide the solutions into 3-km depth bins for inversion to analyze the variation in stress orientation with depth. We use the stress orientations determined in Sub-region A to represent the typical state of stress in the outer forearc.

2.3. Inversion Results

Inverting the outer forearc (Sub-region A) solutions indicates σ_1 is oriented margin-normal, σ_2 is oriented margin-parallel, and σ_3 is sub-vertical. This result is consistent with past studies that the state of stress in the outer forearc is dominated by margin-normal compression from the plate coupling force (e.g., Wang and He, 1999; Balfour et al., 2011). The orientations of σ_2 and σ_3 indicate that the margin-parallel compression is greater than lithostatic (σ_3), which may be

caused by the Oregon push or the margin-parallel component of the plate coupling force. However, the relatively large confidence region of σ_3 and its overlap with that of σ_2 indicate large uncertainties, due possibly to variation in the stress state within this sub-region or an insufficient number of focal mechanism solutions.

The inversion results for the inner forearc regions indicate margin-parallel σ_1, which is consistent with past studies (e.g., Wang and He, 1999; Balfour et al., 2011). The orientations of σ_2 and σ_3 in the inner forearc vary between margin-normal and vertical. In sub-region C, the confidence regions of σ_1 and σ_2 are overlapping. While this may indicate non-uniform stress state or insufficient solutions, the relatively large value of ϕ (0.56) compared to those in other inner forearc sub-regions indicates that σ_2 is closer to σ_1 in magnitude than to σ_3. We interpret this to indicate that (1) the margin-normal compression caused by the coupling force is greater than in other inner forearc sub-regions and/or (2) the magnitude of margin-normal tension due to the gravitational collapse force and the buoyancy of the serpentinized mantle wedge is smaller than in other inner forearc sub-regions. Horizontal σ_2 in neighboring sub-region D indicates a similar relative increase in margin-normal compression due to the coupling force or reduced margin-normal tension. The confidence regions for σ_1 and σ_2 are distinct in sub-region D, which indicates that the magnitude of margin-parallel compression is clearly greater than the margin-normal compression, which is supported by the lower ϕ value (0.3) of the sub region. In Sub-region G, the large confidence regions of σ_3 and its span over most of the confidence region of σ_2

indicate that it is poorly resolved and cannot be reliably distinguished from σ_2. However, the ϕ value is the smallest of all the sub-regions, indicating that the magnitudes of σ_2 and σ_3 are close, which is likely to contribute to difficulty in resolving the two principal stresses. For the other sub-regions in the inner forearc, the relatively small values of ϕ indicate that the magnitude of σ_2 and σ_3 are similar. This has been interpreted to indicate that the magnitudes of the margin-normal compression due to plate coupling and the margin-normal tension due to the gravitational collapse force and/or the buoyancy of the serpentinized mantle wedge corner are similar (Wang and He, 1999). As discussed further in **Section 3**, the buoyancy of the serpentinized mantle wedge corner can generate margin-normal tension at shallow depths.

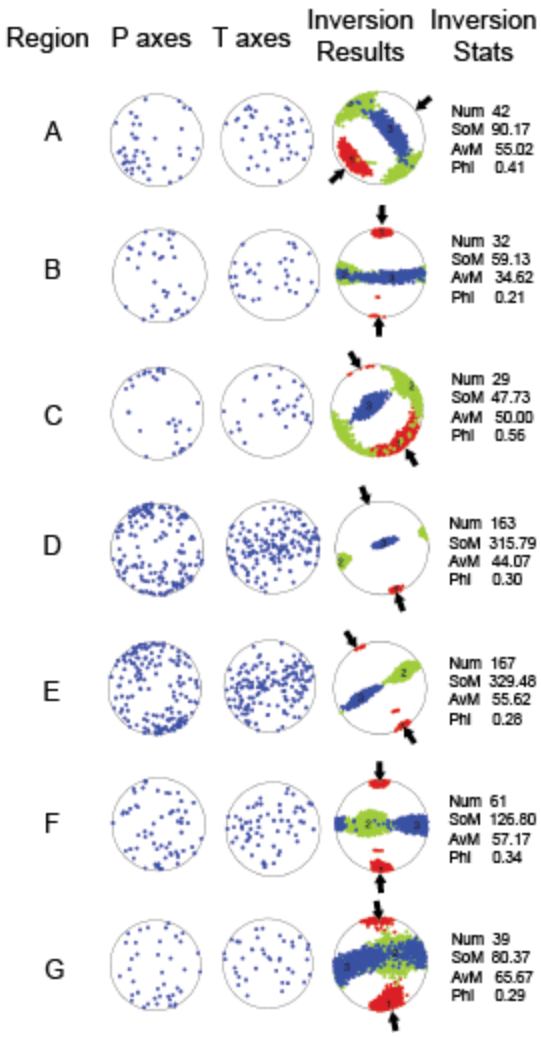

Figure 4. Compressional (P) axes (first column) and tensional (T) axes (second column) of focal mechanisms in sub-regions A–G, and focal mechanism inversion results (third column), all plotted on equal axis lower hemisphere projections. Numerals 1, 2, and 3 on the inversion results indicates σ_1, σ_2, and σ_3, respectively. Clouds of red, green, and blue circles indicate the 95% confidence regions of σ_1, σ_2, and σ_3, respectively. The number of focal mechanism solutions (Num), sum of misfit (SoM), which is 1-cos(β) where β is the angle between the tangential traction predicted by the best stress tensor and the slip direction on each plane, the average of all β for each solution (AvM), and ϕ (phi) are indicated on the right most column.

The orientation of σ_1 is generally margin-parallel throughout the depth column in Sub-regions D-F. Large confidence regions of σ_2 and σ_3 indicate large

uncertainties in their orientations, but σ_2 tends to be sub-horizontal (horizontal compression) for the most part, perhaps except in the 3-6 km depth range. However, the relatively small ϕ values indicate that their magnitudes are similar, indicating that the combined effects of the gravitational collapse force, plate coupling, and/or the buoyant serpentinized zone are causing the “neutral” stress state as observed for most parts of the inner forearc of northern Cascadia.

In the 9-12 km depth bin, the high ϕ value (0.58) and the overlapping confidence regions of σ_1 and σ_2 indicate the magnitude of σ_2 is greater than in the other depth bins, potentially indicating a change in the direction and magnitude of the plate coupling force over this depth range. Alternatively, as proposed by Rey et al. (2001) (**Figure 5**), the gravitational collapse force may cause margin-normal normal faulting near the arc and margin-normal reverse faulting in the forelands closer to Puget Sound, potentially explaining the margin-normal reverse faulting events in the 9-12 km depth bin.

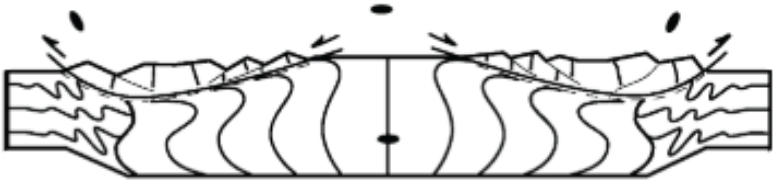

Figure 5. Schematic diagram illustrating deformation due to gravitational collapse (Ray et al., 2001). Gravity acting on high terrain can cause brittle deformation in the upper crust, resulting in normal faulting in high terrain and thrust faulting in low terrain (half arrows). Faulting in the brittle upper crust can occur in combination with ductile deformation in the lower crust or without deformation of the lower crust. Lines within the deforming bodies indicate the sense and magnitude of ductile deformation. Solid ovals are strain ellipses (the result of a strained circle) to indicate the orientation and magnitude of strain at locations within the schematic.

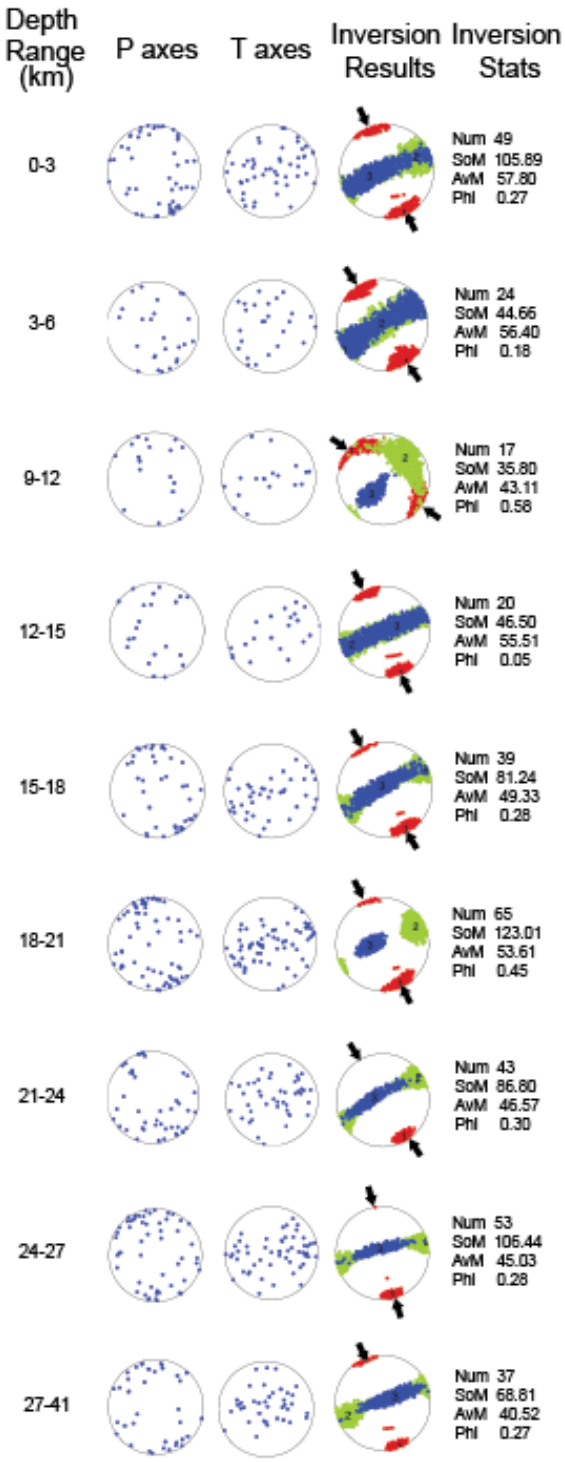

Figure 6. P and T axes of focal mechanism solutions and stress inversion results for 3 km depth bins of inner forearc regions D, E, and F, presented in the same manner as in **Figure 3**.

3. Lithospheric Deformation

3.1. Numerical Modeling Approach

We use the finite-element code PyLith (Aagaard et. Al., 2017) to investigate the sources and magnitudes of the stress field throughout the forearc. PyLith is actively maintained through the community-driven organization, Computational Infrastructure for Geodynamics (https://geodynamics.org/), and has been applied to study lithospheric stresses (e.g., Levandowski et al., 2017). The code solves the conservation of momentum equation:

$$\rho \frac{\partial^2 u_i}{\partial x^2} - f_i - \sigma_{ij,j} = 0 \quad (2)$$

where rho is density, u_i is the displacement vector, f_i is the body force vector, and $\sigma_{ij,j}$ is the divergence of the stress tensor σ_{ij}. For three-dimensional problems, indices *I* and *j* have range 3. We obtain two sets of modeling results: one with a linear elastic rheology and the other with linear viscoelastic rheology. The linear elasticity constitutive relation is given by:

$$\sigma_{ij} = 2\mu\varepsilon_{ij} + \lambda_{kk}\delta_{ij} \quad (3)$$

where σ is the stress tensor, μ and λ are Lamé's constants, ε is the strain tensor, and δ is Kronecker's delta. Lamé's constants are related to the compressional and shear seismic waves (v_p and v_s, respectively) by the following relationships:

$$\mu = \rho v_s^2 \tag{4}$$

$$\lambda = \rho v_p^2 - 2\mu \tag{5}$$

The linear viscoelastic constitutive relation in 1-D is given by:

$$\dot{\varepsilon} = \frac{\sigma}{\eta} + \frac{1}{E}\frac{d\sigma}{dt} \tag{6}$$

where $\dot{\varepsilon}$ is strain rate, η is the viscosity, and E is Young's modulus (**Figure 7**). The volumetric strain is completely elastic in the viscoelastic case. Elastic strain occurs instantaneously, and the stress relaxes with time due to viscous deformation. The viscous deformation becomes more dominant than the elastic deformation at times greater than the Maxwell relaxation time:

$$\tau = \frac{2\mu}{E} \tag{7}$$

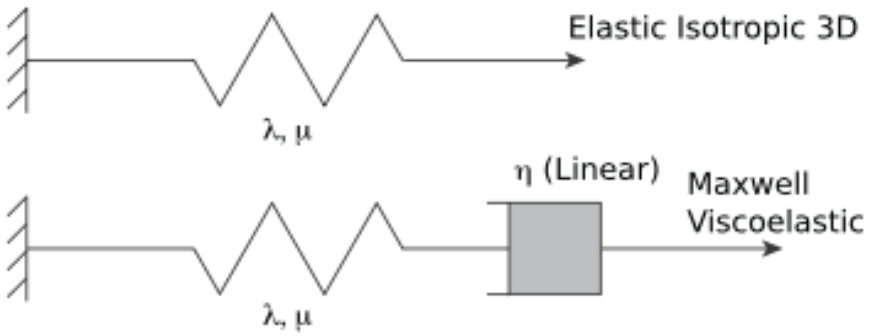

Figure 7. Schematic illustration of linear rheology models used in this study. Elastic isotropic rheology is governed by Lame's constants λ, and μ, and is represented by a spring. Linear viscoelastic rheology is governed by Lame's constants and viscosity and is represented by a spring and a dashpot connected in series.

We use a two-layer rectangular prism model that consists of a 30-km-thick crust and a 70-km thick mantle as a reference model. The model dimensions are 200 km in length in the margin-parallel (x axis) direction, 100 km in width in the margin-normal (y axis) direction, and 100 km in depth in the vertical (z axis) direction. The rest of the models consist of four components, representing the 8-km-thick upper crust, 22-km-thick lower crust, serpentinized mantle wedge corner, and peridotitic upper mantle (**Table 1**). The model components vary in shape to form a range of model geometries that represent a simplified generic forearc system. The simplest model geometry is employed in Models A–D and has the same dimensions as the reference model (**Figure 8a**). In Model A, the upper crust has the same material properties as the lower crust, and the serpentinized mantle wedge corner is a rectangular prism running parallel to the length of the model. Model B is the same as Model A except the serpentinized mantle wedge corner is a triangular prism. Model C only differs from Model B in

that displacement is applied to the “southern” vertical boundary to test the effect of the Oregon push. In Model D, the upper crust and the lower crust have different material properties, and the serpentinized mantle wedge corner is an asymmetric triangular prism. In Models E–G, we use an asymmetric triangular prism model domain where the diagonal face represents the slab surface (**Figure 8b**). In Model E, the upper crust and lower crust have the same properties, and the surface is flat. In Model F, the upper and lower crust have different properties, and the surface elevation increases from zero at the trench to 4000 m at the arc as part of the upper crust component. In Model G, we vary the slab dip from 45° at the margin-parallel ends of the domain to 15° in the center of the domain to approximate the concave-downward shape of the Juan de Fuca slab in northern Cascadia (**Figure 8c**). We use the commercial software Trelis 16.5 to create the finite-element meshes.

Table 1: Model domain, model components, and boundary conditions

Model	Model geometry	Crust	Mantle wedge corner	Oregon push	Basal traction
A	rectangular prism	uniform properties throughout the crust	Rectangular prism	without	without
B	rectangular prism	uniform properties throughout the crust	Triangular prism	without	without
C	rectangular prism	uniform properties throughout the crust	Triangular prism	with	without
D	Rectangular prism	thin upper crust over thick lower crust	Triangular prism	without	without
E	triangular prism	uniform properties throughout the crust	Triangular prism	with	with
F	triangular prism	thin upper crust with sloped topography over thick lower crust	Triangular prism	with	with
G	triangular prism with varied slab dip	uniform properties throughout the crust	Triangular , curved	without	with
H	triangular prism with varied slab dip	uniform properties throughout the crust	Triangular , curved	with	with

We apply a free surface boundary condition to the top surface of each model domain in this study. A free slip boundary condition is applied to the sides and bottoms of the model domains except for the diagonal subduction boundary in Models E–G and the southern vertical boundary in Models C, E, F, and H where we apply a displacement to approximate the effect of the Oregon push. On the diagonal subduction boundary in Models E–G, we apply down-dip shear stress that linearly increases from zero at the surface to a maximum of 12.8 MPa

at 15-km depth and decreases to zero at 20-km depth. The shear stress is calculated by using the friction equation:

$$f_f = \mu N \tag{8}$$

where N is the normal stress on the fault, and μ is the strength of the fault, or effective coefficient of friction. We approximate the normal stress by the lithostatic stress and use 0.03 for the effective coefficient of friction (Wang,1999). We also apply lithostatic stress normal to the diagonal surface to support the model domain. The GPS observations indicate that the Oregon block is moving northward at about 5 mm/yr (McCaffery et al., 2007). We approximate the effect of the Oregon push by applying a displacement of 5 m in the elastic models, representing the cumulative displacement over 1000 years and a velocity of 5 mm/yr in the viscoelastic models, normal to the southern vertical boundary of the model from the surface to 30-km depth; the applied normal displacement or velocity linearly decreases to zero at 50-km depth.

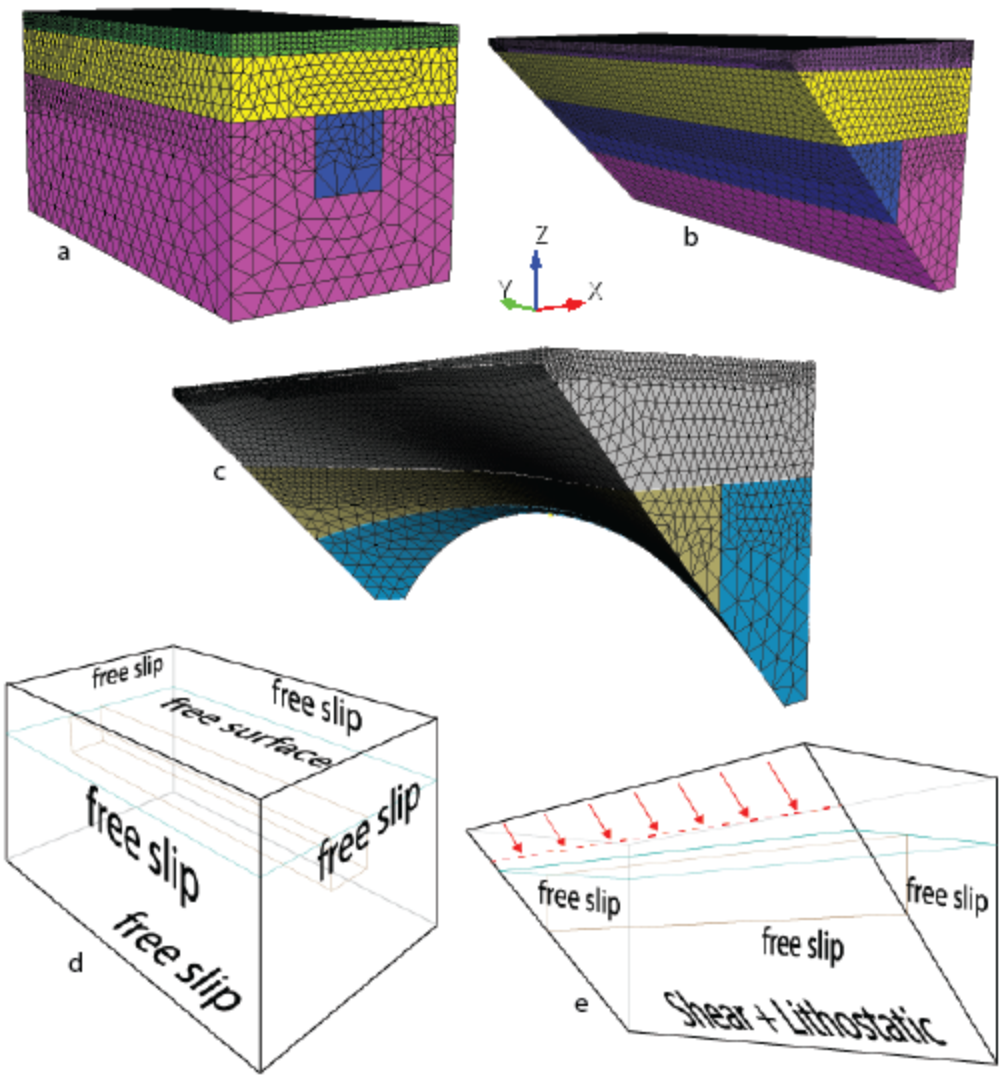

Figure 8. (a–c) Model geometry and an example mesh for 4-component rectangular and triangular prism models (A and F), and a 3-component triangular prism model with varying slab dip angle (G), respectively. Green, yellow, blue, and purple regions represent upper crust, lower crust, serpentinized region, and mantle. **(d, e)** Boundary conditions on Models A–D and E–H, respectively. The red dashed line represents the down dip limit of imposed basal shear stress at 20 km.

For Models A–D, we present two sets of modeling results: one with an elastic rheology and the other with a viscoelastic rheology. The model with the

viscoelastic rheology will be indicated with the prime symbol on the model ID (i.e., A for elastic and A' for viscoelastic models). The elastic properties vary among different model components but are uniform within each component. In PyLith, the elastic properties are defined in terms of P- and S-wave velocities (v_p and v_s, respectively). We use generic values commonly used in the literature for different lithologic components of the models (**Table 2**) to make our results comparable to other works that also use commonly used values. We test the effect of the buoyant mantle wedge corner by varying the mantle wedge density while keeping other parameters the same. We also test the effects of the rheological parameters of the upper crust on the lithospheric deformation (i.e., by changing v_p and v_s).

Table 2: Material properties for Models A–F (Stacy and Davis, 2008)

	Upper ~8 km Crust	Crust	Mantle	Mantle Wedge
Vp [km/s]	5.8	6.8	8.11061	6.5
Vs [km/s]	3.2	3.9	4.49094	3.25
Density (ρ) [kg/m3]	2600	2900	3380	2830
Shear Modulus (μ) [Pa]	2.66E+10	4.41E+10	6.82E+10	2.99E+10
Bulk Modulus (K) [Pa]	5.20E+10	7.53E+10	1.31E+11	7.97E+10
Viscosity (η) [Pa*s]	1.00E+22	1.00E+22	1.00E+19	5.00E+18
First Lamé Parameter (λ) [Pa]	3.42E+10	4.59E+10	8.60E+10	5.98E+10
Young's Modulus (E) [Pa]	6.82E+10	1.11E+11	1.74E+11	7.97E+10
Maxwell Relaxation Time (τ) [s]	2.93E+11	1.81E+11	1.15E+08	1.25E+08
Maxwell Relaxation Time (τ) [y]	9,295.0	5,727.9	3.6	4.0

For Model G, we refer to the Cascadia seismic velocity models reported by USGS (Stephenson, et. al., 2017) and identify representative v_p and v_s for the mantle, crust and upper crust (**Table 3**). For the density of the upper and lower crust and peridotitic mantle, we use an empirical relationship between density and v_p (Brocher, 2005):

$$\rho = 1.6612 * V_p - 0.4721 * V_p^2 + 0.0671 * V_p^3 - 0.0043 * V_p^4 + 0.000106 * V_p^5 \quad (9)$$

The empirical relationship is a nonlinear, multivalued, and quantitative relationship based on v_p, v_s, and density for a wide variety of lithologies using borehole logs, vertical seismic profiles, laboratory measurements, and seismic

tomography models for a diverse dataset to derive the empirical relationship from. For the serpentinized mantle wedge corner we use v_p, v_s, and density values reported for serpentinites (Christensen, 1966) and pure antigorite (Wang, et. al., 2019).

For the given set of v_p, v_s, and viscosity (η), the corresponding Lamé parameter (λ), Young's modulus (E), and Maxwell relaxation time ($\tau = 2\eta/E$) are also summarized in **Table 3**. Maxwell relaxation time is important when modeling viscoelastic behavior as elastic stress decays exponentially with time due to viscous flow. In this study we are focused on defining interseismic forearc stresses. We find the earthquake cycle (~500 years) is much less than the Maxwell relaxation time of the crust (~5000-7000 years), which makes the assumption of an elastic rheology reasonable because viscous deformation is negligibly small on the time scale of our study.

Table 3: Material Properties for Models G and H

	Crust	Mantle	Mantle Wedge	Upper ~8 km Crust
Vp [km/s]	6	7.3	6.5	5
Vs [km/s]	3.6	3.9	3.25	3.1
Density (ρ) [kg/m3]	2717	3058	2830	2535
Shear Modulus (μ) [Pa]	3.52E+10	4.65E+10	2.99E+10	2.44E+10
Bulk Modulus (K) [Pa]	5.09E+10	1.01E+11	7.97E+10	3.09E+10
Viscosity (η) [Pa*s]	1.00E+22	1.00E+19	5.00E+18	1.00E+22
First Lamé Parameter (λ) [Pa]	2.74E+10	6.99E+10	5.98E+10	1.47E+10
Young's Modulus (E) [Pa]	8.58E+10	1.21E+11	7.97E+10	5.79E+10

Maxwell Relaxation Time (τ) [s]	2.33E+11	1.65E+08	1.25E+08	3.46E+11
Maxwell Relaxation Time (τ) [y]	7389.0	5.2	4.0	10958.3

3.2. Model Sensitivity to Parameters

In this section, we aim to describe the changes in the magnitudes of displacement and stress with model parameters. Given that the numerical experiments that are conducted are exploratory and that there are a large amount of numerical data compared to the scope of this study, the magnitude values that are provided below are obtained through visual inspections of **Figures 9–15** only and are approximate, which is sufficient to provide the sense of changes in the displacement and stress with model parameters. Further, there are a number of model behaviors that are difficult to explain as pointed out below. Although these add significant uncertainties, we present the results as work-in-progress.

To investigate the effects of various forces, we first develop a simple two-layer model that consists of the overriding crust and the mantle with no lateral variation in density and is laterally confined (**Figure 9**). Ideally, in this reference model, the elevation and stress at the surface are zero, and the state of stress is lithostatic everywhere. However, upon application of gravity to the model domain in PyLith, the material compresses vertically, resulting in down-ward displacement by 26 m (subsidence). This causes horizontal compression, ranging from -8 to -24 MPa, even at the surface, and despite the fact that the surface is treated as a free surface without overriding material, the vertical stress

at the surface is identical to that of the horizontal stress (i.e., vertical compression). Note that negative stress values indicate compression as in the continuum mechanics convention. The cause of the non-zero and non-uniform stress at the surface is unknown, and the application of gravity in PyLith requires further testing. In the following, we investigate the effects of model parameters relative to the surface elevation and the compressive state of stress of this reference model, assuming that all models experience the same effect of gravity.

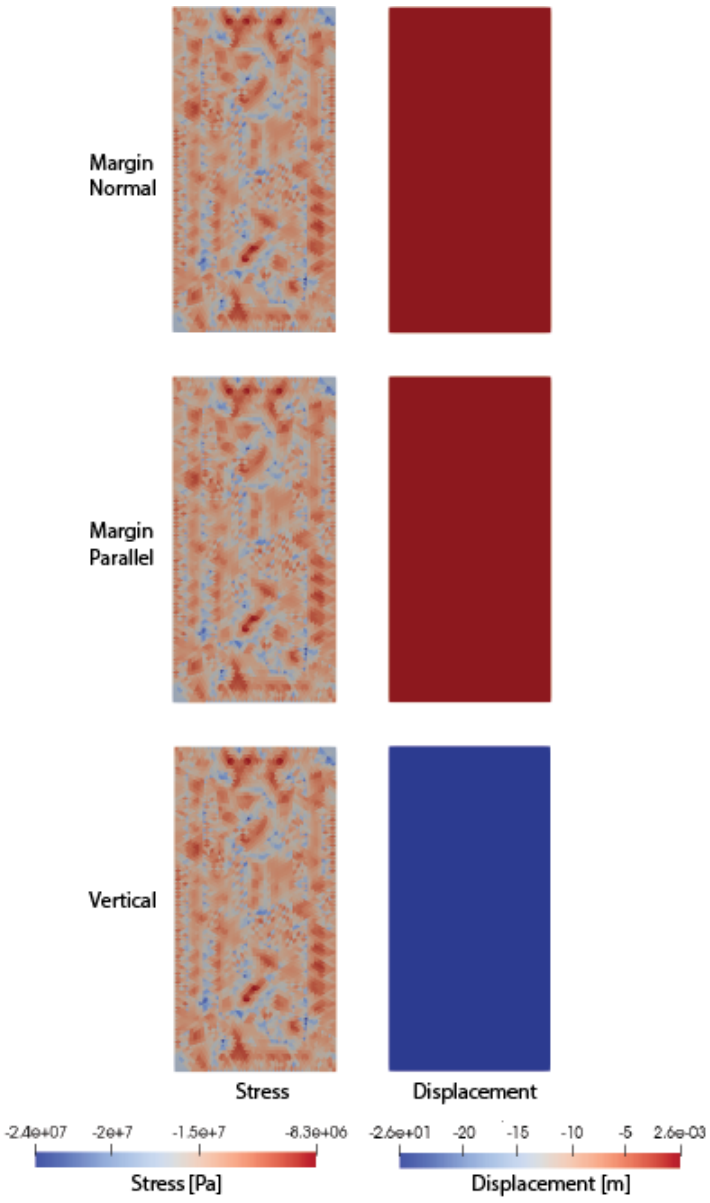

Figure 9. (left column) Stress magnitude and (right column) displacement at the surface in (top) the x direction, (middle) the y direction, and (bottom) the z direction in map view for the reference model with an elastic rheology. Each panel represents the full lateral dimensions of the model (i.e., 100 km by 200 km). Negative stress values indicate compression.

We use Model A to test the effects of the buoyant mantle wedge. It is our simplest case where the model consists of a symmetric body of serpentinized

mantle rock sandwiched between a 30-km thick continental crust and lithospheric mantle in a rectangular prism (**Figure 8a**). The elastic crust flexes upward above the buoyant serpentinized zone. This results in margin-normal displacement at the surface away from the serpentinized zone toward the edges of the domain, with peak displacements of 3 m directly above the edges of the serpentinized zone in Model A (**Figure 10**). Upward flexing is also indicated by the upward surface displacement above the serpentinized zone; although the displacement value is -7.5m, relative to the reference model with -26 m (downward) displacement, the surface experiences a 18.5 m uplift (**Figures 10 and 11c**). Relative to the state of stress in the reference model, Model A experiences margin-normal tension (+20 MPa) above the serpentinized zone and greater margin-normal compression (-15 MPa) at the surface near the arc and trench side vertical boundaries of the model domain (**Figure 12a**). The tension is caused by the upward flexing of the crust. The margin-normal compression at the trench- and arc-side boundaries is due to the imposed boundary conditions that do not allow displacement in the margin-normal direction.

We test whether a linear elastic rheology is a reasonable approximation of the more realistic viscoelastic rheology, using Models A and A' (**Figure 10**). The displacement and stress values in Model A' after 500 years of loading are compared to the results of Model A. This loading time is chosen to reflect the average megathrust earthquake recurrence interval in Cascadia. Stress orientations and magnitudes and displacement directions are identical between the two models. This occurs because elastic deformation is instantaneous while

the viscous relaxation time of the crust is much longer, ~7400 years (**Table 3**). These results indicate that an elastic rheology is a reasonable approximation for this study.

Although the sense of displacements are consistent between Models A and A', the magnitude of displacement is exactly six-orders of magnitude larger in the viscoelastic model than in the elastic model. The cause of this discrepancy is unknown and needs to be addressed in future work.

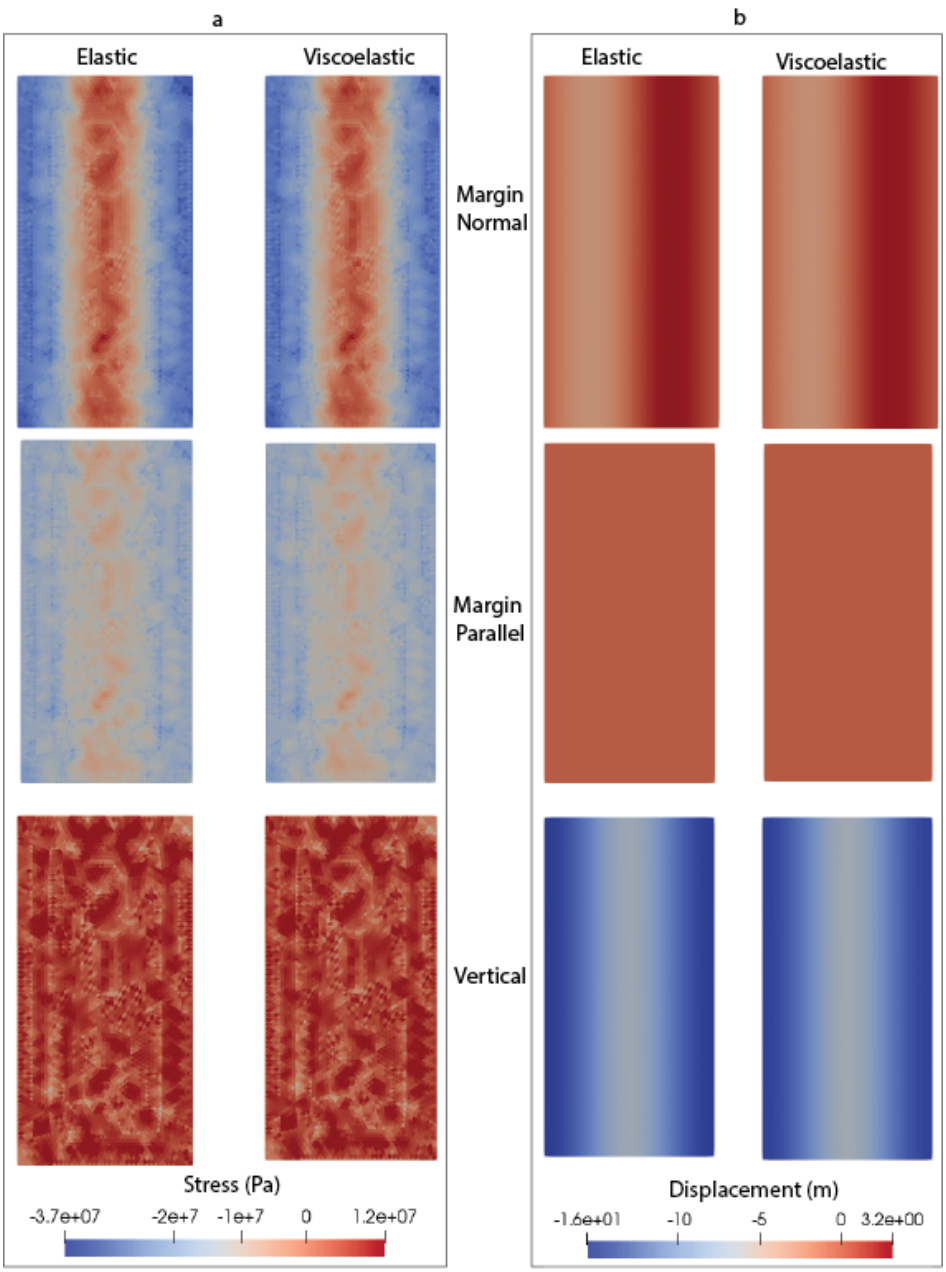

Figure 10. (a) Stress magnitude and **(b)** displacement at the surface in (top) the x direction, (middle) the y direction, and (bottom) the z direction in map view for Models A (elastic) and A' (viscoelastic). Note the magnitude of displacement for Model A' is exactly 6 orders of magnitude larger than the displacement magnitudes for Model A (see text).

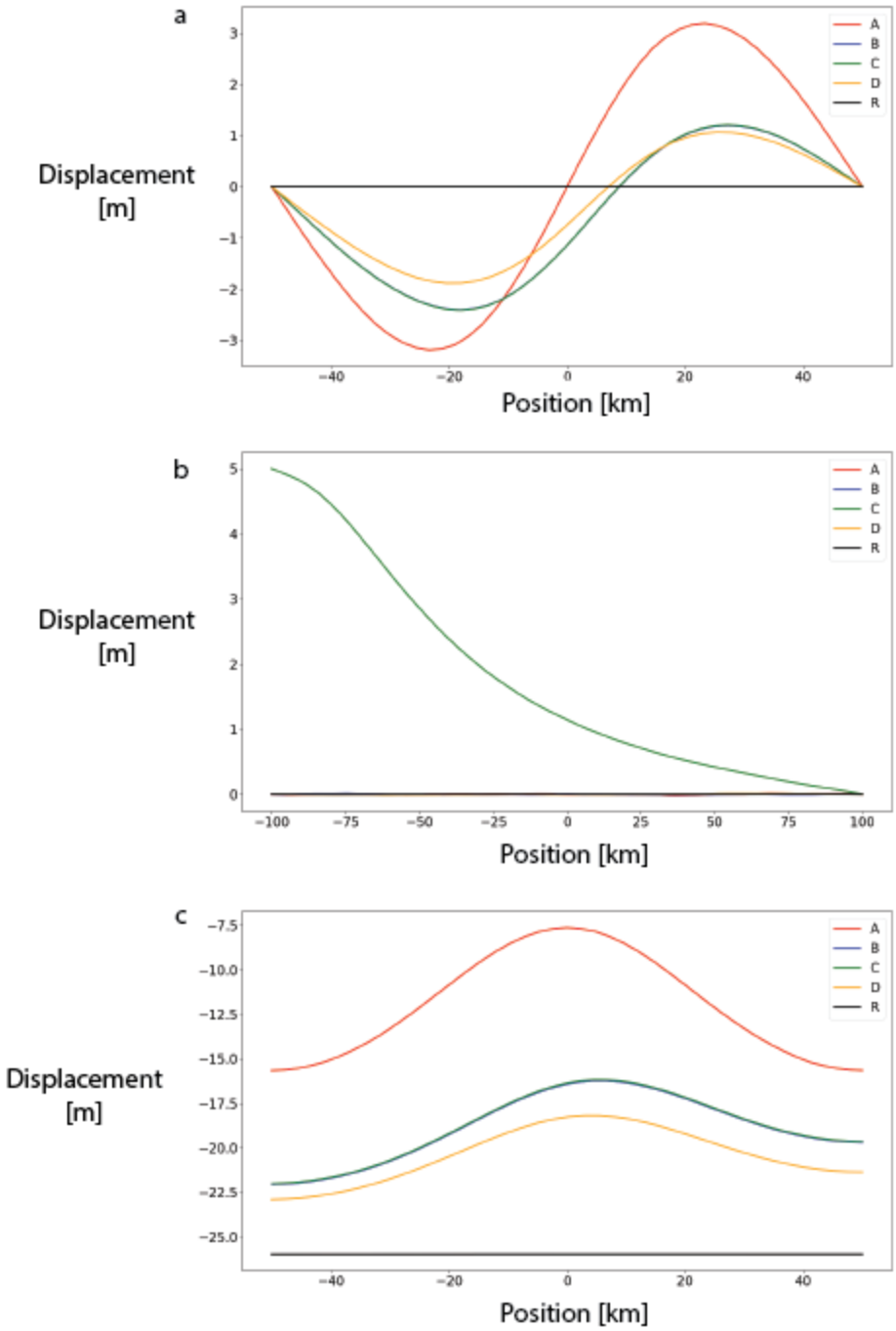

Figure 11. Displacement at the surface: (a) x-component along a margin-normal profile, (b) y-component along a margin-parallel profile, and (c) z-component along a margin-normal profile for Models A–D and the reference model (R). Margin-normal displacement is directed away from the center (buoyant serpentinized region) in all cases. Models B and C are overlapping in (a), all models except C are overlapping in (b), and Models B and C are overlapping in

(c). The displacements in Model A'–D' with a viscoelastic rheology are 6 orders of magnitude larger than the displacement magnitudes in Model A–D (see text) and are not shown.

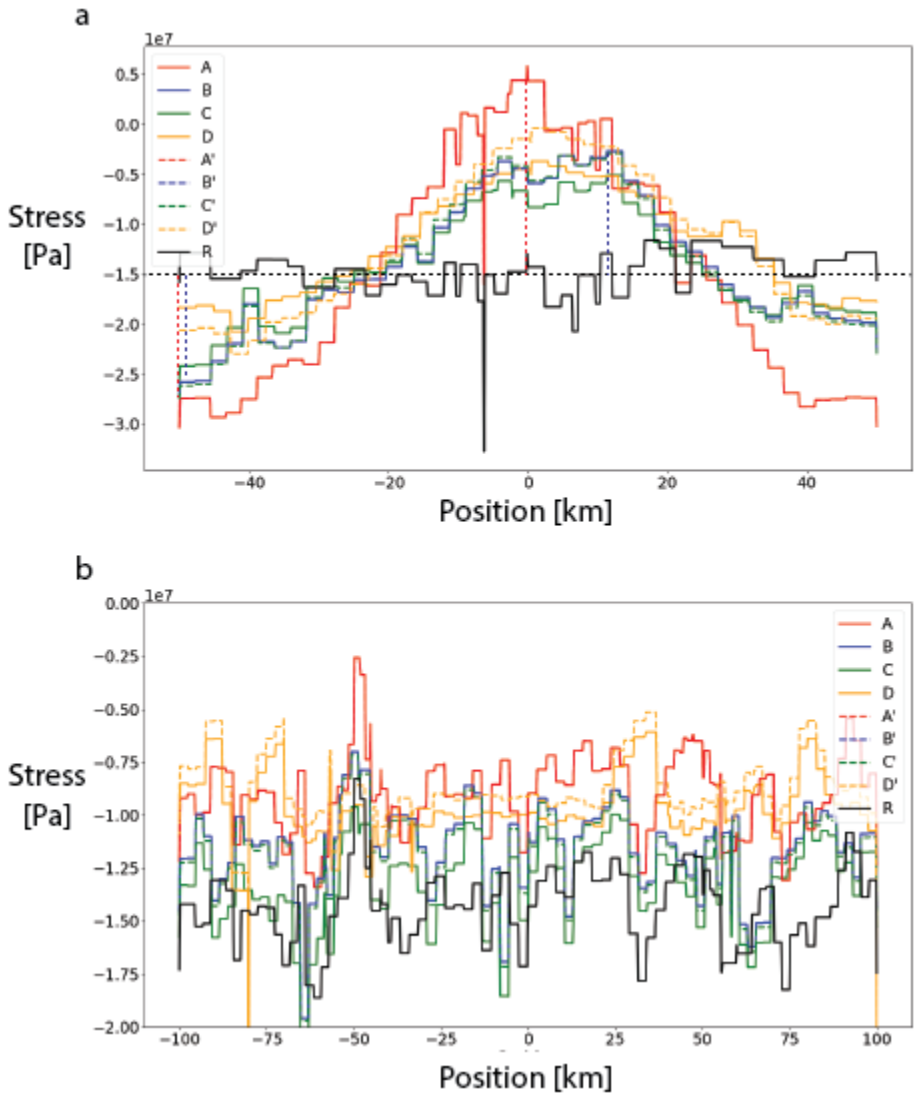

Figure 12. (a) Margin-normal stress along a margin-normal profile and (b) margin-parallel stress along a margin-parallel profile for Models A–D, A'–D', and the reference model (R). Except for Models D and D', the elastic and viscoelastic results are overlapping. Black dashed line is the average stress of the reference model (R) which we use as a baseline. Red and blue vertical dashed lines denote the positions from which we glean peak tension and compression values for Models A and B, respectively.

We use Model B to test the effect of a wedge-shaped serpentinized zone. In this case the serpentinized zone is an asymmetric triangular prism, running the margin-parallel length of the domain, and is thinnest on the trenchward side and thickest on the arc-ward side (**Figure 8b**). Peak margin-normal displacements (both negative and positive) at the surface are slightly shifted arc-ward relative to the displacements of Model A (**Figure 11a**). The peak upward displacement above the serpentinized zone is reduced from 18 m in Model A to 10 m in Model A', but it is still an uplift relative to the reference model (**Figure 11c**). The margin-normal tension at the surface is also reduced from 20 MPa in Model A to 12 MPa in Model B (**Figure 12a**). Compression at the trench-side vertical boundary is similar but at the arc-side vertical boundary is reduced by 8 MPa (**Figure 12a**)**.** This result indicates that the presence of a serpentinized mantle wedge can cause tension in the overriding crust at shallow depths (if serpentinization occurs at a shorter time scale than the relaxation time of the crust).

We use Model C to test the effect of the Oregon push. The model domain is identical to Model B, but the Oregon push boundary condition is imposed on the "southern" vertical boundary of the domain. The margin-normal and vertical displacements at the surface are nearly identical to Model B. The margin-parallel displacement at the surface (**Figure 11**) peaks (5 m) at the southern boundary where the displacement is imposed and reduces to zero at the opposite boundary. The margin-normal stress is more tension over the serpentinized mantle wedge and less compression near the trench- and arc-side boundaries.

The magnitude of margin-parallel compression at the surface is slightly larger than that of Model B throughout the model domain , particularly near the southern boundary (**Figure 12b**). The shortening by 5 m over the 200-km length of the model causes 5 MPa compression; the effect of the Oregon push is only half the effect of the buoyancy of the serpentinized mantle wedge in magnitude (10 Ma tension).

We use Model D to test the effect of vertical density variation within the overriding crust. Model D is identical to Model B except that the 8-km thick upper crust has rheological properties that are distinct from that of the lower crust (**Table 2**). Margin-normal displacements (**Figure 11**) at the surface are similar to Model B, but with slightly smaller maximum magnitudes (0.5 m smaller on the trenchward side and 0.2 m smaller on the arc-ward side). Margin-parallel displacement is zero throughout the domain similar to Models A and B. In this case margin-normal tension at the surface is similar to that of Model B above the thick side of the serpentinized zone near the center of the domain and along the back-arc-side boundary of the domain (**Figure 12**). Margin-normal compression along the trench-side vertical boundary is of a lower magnitude than Model B. In this model, the triangular buoyant mantle wedge causes less vertical flexing of the overriding crust (i.e., less uplift; **Figure 11**), which leads to less uplift across the domain, and less compression at the side boundaries, relative to Model B. The magnitude of margin-parallel compression is smaller than Models A–C due to the relatively low density of the upper crust.

Unlike Models A–C, Model D' with the viscoelastic rheology differs from Model D with the elastic rheology. Compared to Model D, the magnitude of margin-normal tension at the surface above the serpentinized zone is larger in Model D', and the magnitude of margin-normal compression along the trench and arc boundaries is also larger (by 2-3 MPa). Margin-parallel tension is greater (less negative value) at the surface in Model D' (by 2-3 MPa). The reason for the differences between Models D and D' is unclear.

We use Model E to test the effects of basal shear. Model E is bounded at the bottom by a 45° dip subduction interface and consists of a 30-km thick continental crust, lithospheric mantle and a serpentinized mantle wedge corner (**Figure 2c**). At the trench-side edge of the model, there is a short vertical boundary that extends from the surface to 3-km depth, which intersects with the up-dip end of the dipping subduction interface. We impose lithostatic pressure on this vertical boundary. Along the subduction interface, down-dip oriented basal shear stress and interface-normal lithostatic pressure are applied. The magnitudes of the basal shear stress and lithostatic pressure are functions of depth as described in **Section 3.1**. The Oregon push boundary condition is imposed on this model as in Model C. Model E is the upper triagonal domain of Model C with basal shear along the diagonal surface.

In Model E, at the trench-side boundary, the surface moves towards the arc due to the effect of basal shear (**Figure 13a**). Margin-normal displacement **(Figure 13)** reaches a maximum value of nearly 200 m arc-ward ~20 km from the trench-side vertical boundary and tapers to ~0 m near the arc-side vertical

boundary. Margin-normal stress at the surface is zero at the trench-side vertical boundary as prescribed. Margin-normal tension **(Figure 14)** at the surface near the trench is due to the increasing arc-ward displacement away from the trench, resulting in stretching, reaching a maximum (200 MPa) 10 km from the trench. We suspect the boundary conditions around the toe of the forearc causes the displacement gradient. Further away from the trench, the outer forearc is under margin-normal compression, which reaches a maximum (500 MPa) 40 km from the trench. The margin-normal compression at the surface decreases towards the arc as a result of increasing distance from the imposed shear, and the state of stress transitions to tension in the inner forearc due to the buoyant serpentinized zone. Margin-parallel displacement is directed northward in the southern half of the domain and is directed southward in the northern half of the domain; the cause of the opposing sense of displacement between the southern and northern halves of the model is unclear, but as shown below, this sinusoidal pattern of margin-parallel displacement occurs for the other triangular prism models (F–H) and is likely related to the boundary conditions. Margin-parallel stress is in compression across the domain. The magnitude of compression at the surface is greatest at the center of the domain (~130 MPa) and smallest(~110 MPa) near the north and south vertical boundaries.

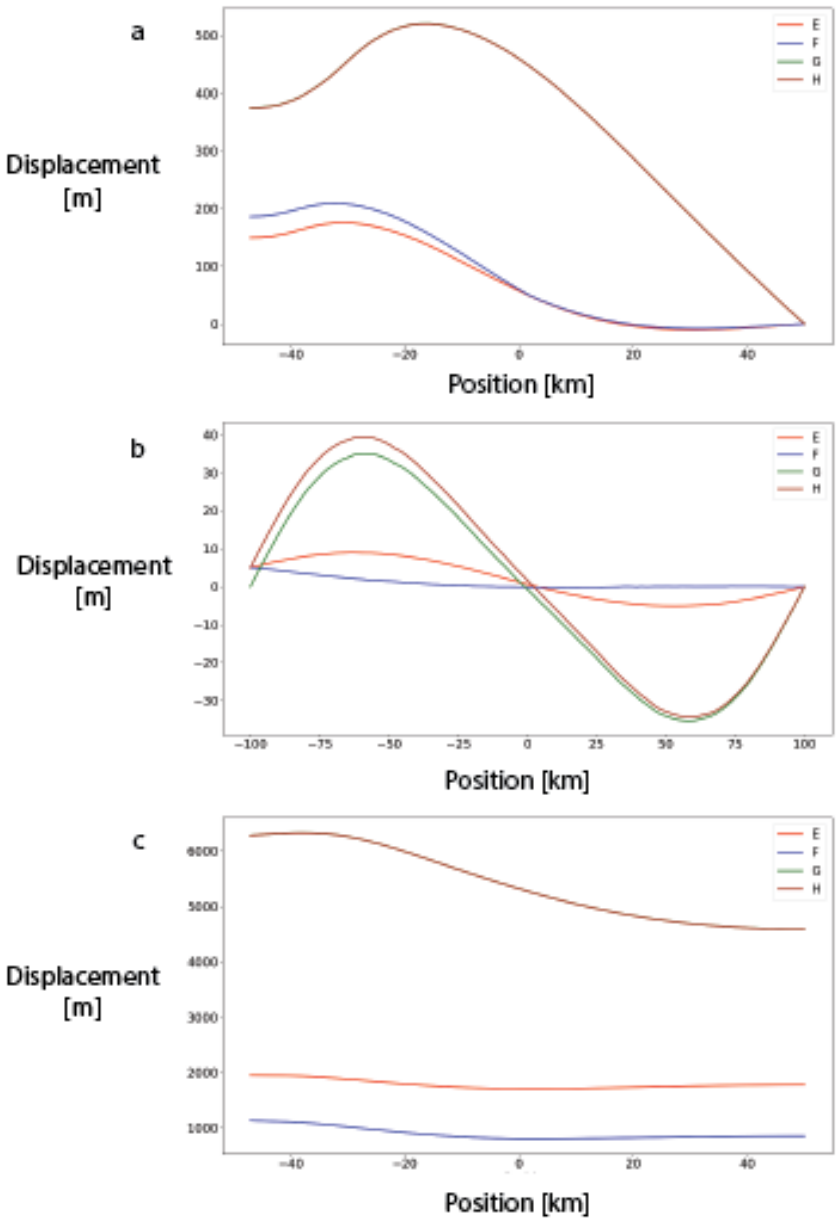

Figure 13. Displacement at the surface: (a) x-component along a margin-normal profile, (b) y-component along a margin-parallel profile, and (c) z-component along a margin-normal profile, for Models E–H. Values for G and H overlap.

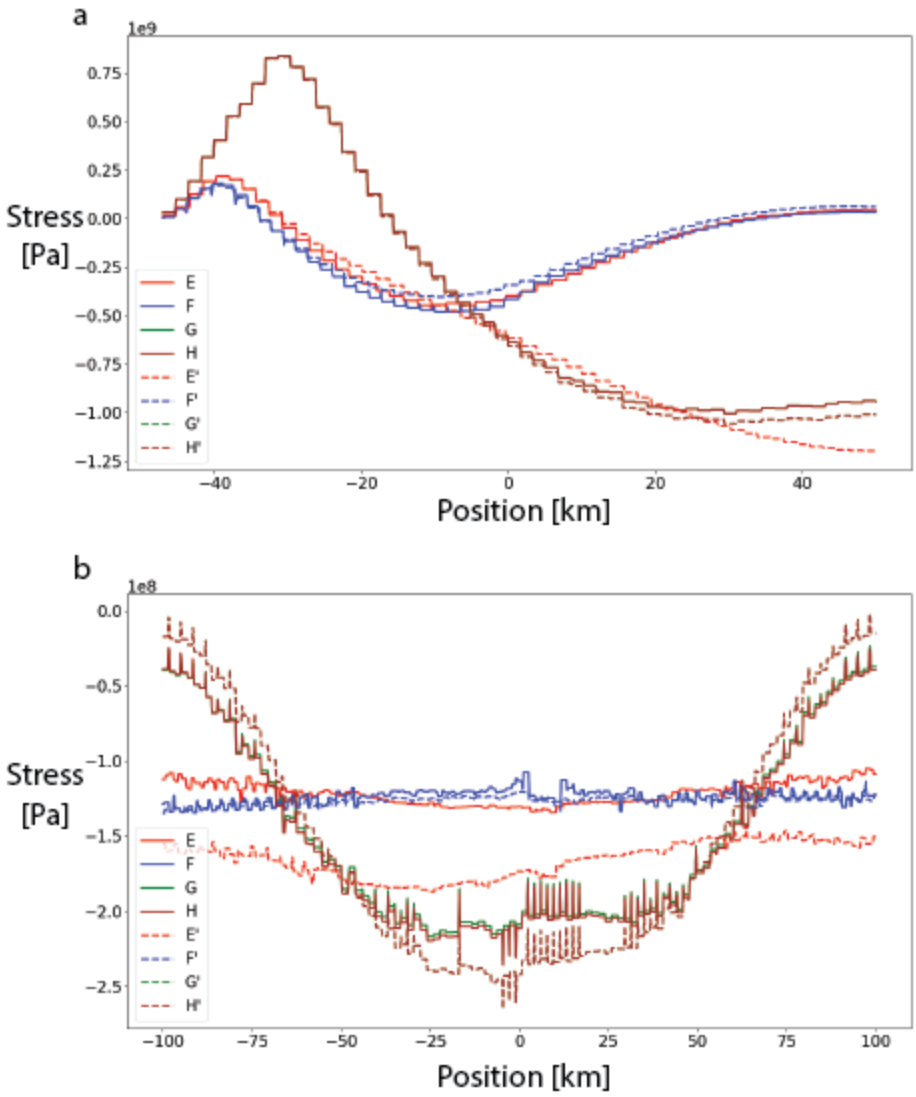

Figure 14. Magnitudes of **(a)** margin-normal stress along a margin-normal profile line and **(b)** margin-parallel stress along a margin-parallel profile line at the surface for Models E–H. Results of elastic rheology models are plotted as solid lines, and viscoelastic rheology models are plotted as dashed lines. Values for G and H overlap.

We use Model F to test the effects of the gravitational collapse force. Relative to Model E, the surface elevation increases linearly from 0 at the trench-side vertical boundary to 4 km at the arc-side vertical boundary. The added

terrain has the same rheological properties as the upper crust (**figure 2d**). Margin-normal displacement **(Figure 13)** follows the same pattern as Model E, but with smaller magnitudes, reaching a maximum of 100 m 20 km from the trench-side vertical boundary. Relative to Model E, margin-normal tension near the trench is reduced **(Figure 14)**, compression in the central part of the outer forearc is reduced, and tension in the inner forearc is increased. Stress magnitudes are within 30 MPa of Model E's magnitudes across the domain. The gravitational collapse force brings the state of stress slightly more margin-normal tension, consistent with previous definitions of stresses due to gravitational collapse (Rey et al., 2001). Margin-parallel displacement is 5 m northward at the southern vertical boundary as prescribed, diminishes to 0 m 75 km from the boundary, and remains at 0 across the remainder of the domain. Margin-parallel compression is greatest (~130 MPa) near the southern boundary, and the magnitude of compression decreases to 110 MPa 50 km from the southern boundary and remains nearly constant throughout the remainder of the domain. The surface elevation is lower than Model E; the cause is unknown.

We use Model G to test the effects of a downward concave slab structure similar to the slab structure of northern Cascadia. In this model we use material parameters unique to Cascadia rather than the generic material parameters used in the other models (**Table 3**). We create the concave-down structure by varying the slab dip from 45° at the southern and northern vertical boundaries to 15° in the center. Margin-normal displacement is directed arc-ward across the domain, with the highest magnitude of displacement, ~500 m, ~30 km from the trench

(**Figure 13a**). Margin-normal tension near the trench occurs over a much wider region and is much greater in magnitude (by 500-800 MPa) in Model G than Model E. This is likely due to the shallower dip of the interface and the wider coupled zone causing a greater displacement gradient over a wider region. This displacement gradient, predicted also by Models E and F, is not observed in real subduction systems, likely indicating that the boundary conditions require further adjustment. The state of stress transitions to compression at ~30 km from the trench, reaching a maximum of 900 MPa 20 km from the arc-side vertical boundary. Here, the stress effect of the serpentinized mantle wedge is completely overshadowed by the effect of plate coupling force.

Margin-parallel displacement is directed toward the center of the domain with maximum displacements being 40 m at 60 km to the north and south of the margin-normal centerline of the domain. This displacement pattern is likely related to the application of gravity, but the effect is spatially varying due to the curved geometry of the bottom boundary unlike in Model A and other applied forces. Margin-parallel stress is in compression across the domain. Maximum margin-parallel compression is 200 MPa in the center of the domain, and minimum magnitudes are 40 MPa at the northern and southern vertical boundaries.

Vertical displacement along a margin-normal line through the center of the domain is directed upward by 6200 m near the trench-side vertical boundary decreasing to 4500 m at the arc-side vertical boundary. The pattern of vertical displacement across the domain is similar to that of Models E and F, but the

magnitude is much larger in Model G. This could be caused by the vertical support at the base of the model being greater than the lithostatic stress and/or the wider coupled zone relative to Models E and F causing shortening and uplift. Vertical displacement along a margin-parallel profile through the center of the domain is uniformly upward at 5500 m (results not shown).

We use Model H to test the effects of the Oregon push on Model G. Modelling results for Model H are nearly identical to Model G. This suggests that the Oregon push has a negligible effect on the stress field relative to the shape of the slab, and this casts doubt on the idea that the Oregon push is the source of stress responsible for the observed seismicity in Cascadia.

Maximum margin-normal and margin-parallel compression in Models G and H is focused above the center of the concave downward slab structure (**Figure 15**). Margin-parallel tension is focused in the northern and southern corners along the arc-ward vertical boundary (1.7 GPa). The location above the concave down slab structure where margin-normal and margin-parallel compressive stresses are focused is the location of the highest density of earthquake events in Cascadia (**Figure 2).** This suggests that despite the measurable northward push of the Oregon block, the margin-parallel compression indicated by focal mechanism inversion may be the result of the slab shape.

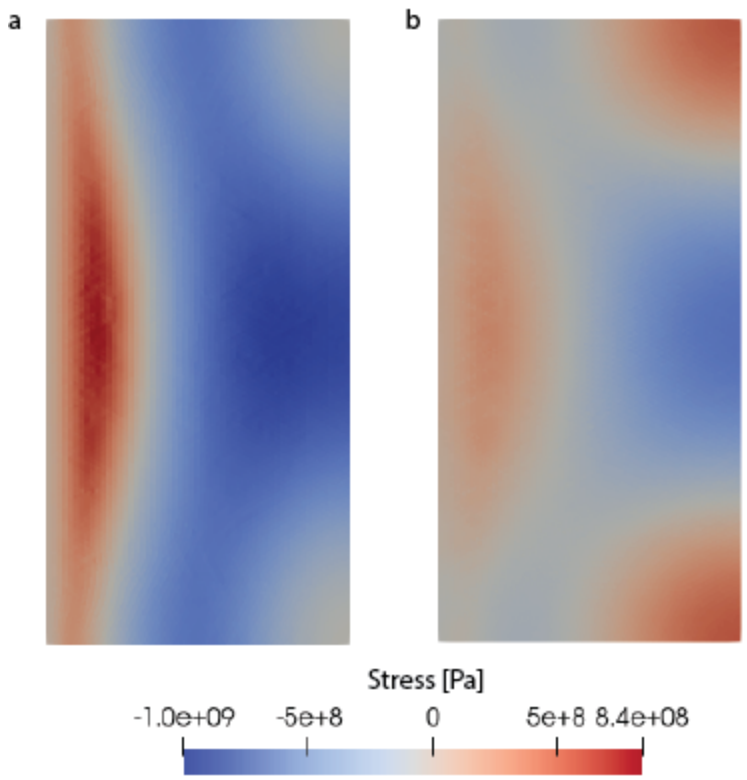

Figure 15. (a) Margin-normal and (b) margin-parallel surface stress in map view in Model H. Compressive stress (blue) is greatest in the forearc above the concave downward slab structure.

4. Discussions and Conclusions

We systematically invert focal mechanism solutions in sub-regions of the Cascadia inner forearc and find that the maximum compressive stress is generally oriented margin-parallel whereas the orientations of the minimum and intermediate compressive stresses vary between sub-vertical to margin-normal both laterally and vertically. These results are in agreement with Balfour (2011) and McCaffrey (2007), which propose that the northward push of the Oregon block is the source of margin-parallel compression in the Cascadia forearc. Subtle variations in the minimum and intermediate compressive stresses indicate

stresses arising from a complex interplay between plate coupling, gravitational collapse force, and the buoyant serpentinized zone, but given the low phi values, the combined effect of gravitational collapse force and the buoyant serpentinized mantle are similar in magnitude to that of the plate coupling force, giving rise to the neutral state of stress.

Our modelling efforts focus on characterizing the state of stress due to the buoyancy of the serpentinized zone, the Oregon push, the plate coupling force, the gravitational collapse force, and the shape of the slab. Our modeling results indicate that the Oregon push generates margin-parallel compression on the order of 100 MPa and that the plate coupling force generates margin-normal compression on the order of 500 MPa. Theses stress magnitudes are much larger than expected for earthquake stress drops and magnitudes suggested by other modeling studies (Wang and He, 1999), and should be investigated further. We find that the effect of the gravitational collapse force on a gently sloped terrain has a relatively small impact on the stress state across the domain, and that the buoyancy of the serpentinized mantle wedge corner has potentially greater effects on the state of stress near the surface and on the topography in the forearc. In all Models A–D, the presence of the serpentinized mantle wedge results in margin-normal tension at the surface.

As previously reported, Cascadia is a low stress subduction zone where the plate coupling force is weak and the forearc stress state is not dominated by margin-normal compression (Wang and He, 1999). This partly explains the lack of seismicity throughout most of Cascadia, but it makes the existence of dense

seismicity in the Puget Sound area perplexing. Past studies (e.g. Balfour, 2011) suggest that the Oregon push is the source of seismogenic stress in the area, largely because the Oregon push compression is oriented in the same direction as compression orientations indicated by focal mechanism inversion. However, this does not explain why seismicity is focused in the Puget Sound area. Our modelling results suggest the concave downward shape of the subducting slab may focus compression in the crust over the curved slab structure, the same location we observe an abundance of seismicity in Cascadia. Future efforts are needed to explore the relationship between slab shape, stress field, and seismicity in Cascadia.

There are a couple of challenges that we face in this study. One is the sparsity of earthquakes throughout the length of the subduction zone, which resulted in relatively large uncertainties in the stress orientation. This study can be revisited on a decadal scale to update the state of stress using a new compilation of focal mechanism solutions. The other is the design of the model geometry and the application of initial and boundary conditions in PyLith. Our model domains that include a diagonal subduction interface are troubled by issues of supporting the domain against the force of gravity on the diagonal face. The shape of the crustal toe, which is required to avoid numerical problems, causes unrealistic stress effects. These issues can perhaps be addressed by including the subducting slab in the domain and increasing the size of the domain such that the study area is further from the vertical boundaries of the domain.

5. References

Aagaard, B., M. Knepley, C. Williams (2017), PyLith v2.2.1, Computational Infrastructure for Geodynamics, doi: 10.5281/zenodo.886600, url: https://geodynamics.org/cig/software/pylith/

Balfour, N. J., J. F. Cassidy, S. E. Dosso, and S. Mazzotti (2011), Mapping crustal stress and strain in southwest British Columbia, *J. Geophys. Res. Solid Earth*, *116*(3), 1–11, doi:10.1029/2010JB008003.

Boyarko, D. C., M. R. Brudzinski, R. W. Porritt, R. M. Allen, and A. M. Tréhu (2015), Automated detection and location of tectonic tremor along the entire Cascadia margin from 2005 to 2011, *Earth Planet. Sci. Lett.*, *430*, 160–170, doi:10.1016/j.epsl.2015.06.026.

Brocher, T.M., 2005, Empirical relations between elastic wavespeeds and density in the Earth's crust: Bulletin of the Seismological Society of America, v. 95, no. 6, p. 2081– 2092.

Christensen, N. I. (1966), Elasticity of Ultrabasic Rocks, *J. Geophys. Res.*, *71*(24), 5921–5931, doi:10.1029/JZ071i024p05921.

Earthquakes Canada, GSC, Earthquake Search (On-line Bulletin), AutoDRM@seismo.NRCan.gc.ca, Nat. Res. Can., {13 Sep 2019}.

James, T. S., J. J. Clague, K. Wang, and I. Hutchinson (2000), Postglacial rebound at the northern Cascadia subduction zone, *Quat. Sci. Rev.*, *19*(14–15), 1527–1541, doi:10.1016/S0277-3791(00)00076-7.

Kao, H., S.-J. Shan, A. Bent, C. Woodgold, G. Rogers, J.F. Cassidy, and Ristau, J. (2012). Regional centroid-moment-tensor analysis for earthquakes in Canada and adjacent regions: An update, Seismol. Res. Lett., v83, 505-515.

Levandowski, W., M. Zellman, and R. Briggs (2017), Gravitational body forces focus North American intraplate earthquakes, Nat. Commun., 8, 1–9, doi:10.1038/ncomms14314.

McCaffrey, R., A. I. Qamar, R. W. King, R. Wells, G. Khazaradze, C. A. Williams, C. W. Stevens, J. J. Vollick, and P. C. Zwick (2007), Fault locking, block

rotation and crustal deformation in the Pacific Northwest, *Geophys. J. Int.*, *169*(3), 1315–1340, doi:10.1111/j.1365-246X.2007.03371.x.

McCrory, B. P. a, J. L. Blair, D. H. Oppenheimer, S. R. Walter, U. S. G. Survey, and M. Park (2006), Depth to the Juan de Fuca Slab Beneath the Cascadia Subduction Margin — A 3-D Model for Sorting Earthquakes, *U.S. Geol. Surv. Data Ser.*, *91*(2), 1–13, doi:Cited By (since 1996) 14\nExport Date 22 September 2011.

Michael, A. J. (1984), Determination of stress from slip data: Faults and folds, *J. Geophys. Res.*, *89*(B13), 11517, doi:10.1029/JB089iB13p11517.

Michael, A. J. (1987), Use of focal mechanisms to determine stress: A control study, *J. Geophys. Res.*, *92*(B1), 357–368, doi:10.1029/JB092iB01p00357.

Mulder, T. (1995), Small earthquakes in southwestern British Columbia (1975–1991), Ph.D. thesis, Univ. of Victoria, Victoria, B. C., Canada.

Ramachandran, K., R. D. Hyndman, and T. M. Brocher (2006), Regional P wave velocity structure of the Northern Cascadia Subduction Zone, *J. Geophys. Res. Solid Earth*, *111*(12), 1–15, doi:10.1029/2005JB004108.

Rey, P., O. Vanderhaeghe, and C. Teyssier (2001), Gravitational collapse of the continental crust: Definition, regimes and modes, *Tectonophysics*, *342*(3–4), 435–449, doi:10.1016/S0040-1951(01)00174-3.

Stacey, F., and P. Davis (2008), *Physics of the Earth*.

Stephenson, W. J., N. G. Reitman, and S. J. Angster (2017), P- and S-wave velocity models incorporating the Cascadia subduction zone for 3D earthquake ground motion simulations—Update for Open-File Report 2007–1348, *USGS Open File Rep. 2017-1152*, (September), 17, doi:10.3133/ofr20171152.

Trelis (Version 16.5) [Computer software]. American Fork, UT: csimsoft. Retrieved from http://csimsoft.com

U.S. Geological Survey, 2019, Earthquake Catalog, accessed via Libcomcat on September 13, 2019 (https://github.com/usgs/libcomcat)

Wang, K. (1996), Simplified Analysis of horizontal stresses in a buttressed forearc sliver at an oblique subduction zone, *Geophys. Res. Lett.*, *23*(16), 2021–2024.

Wang, K., and J. He (1999), Mechanics of low-stress forearcs: Nankai and Cascadia, *J. Geophys. Res.*, *104*(B7), 15191, doi:10.1029/1999JB900103.

Wang, D., T. Liu, T. Chen, X. Qi, and B. Li (2019), Anomalous Sound Velocities of Antigorite at High Pressure and Implications for Detecting Serpentinization at Mantle Wedges, *Geophys. Res. Lett.*, *46*(10), 5153–5160, doi:10.1029/2019GL082287.

Wells, R. E. (1998), Fore-arc migration in Cascadia and its neotectonic significance, *Geology*, *26*(8), 759–762, doi:10.1130/0091-7613(1998)026<0759:FAMICA>2.3.CO;2.

Yoshida, K., A. Hasegawa, and T. Okada (2015), Spatial variation of stress orientations in NE Japan revealed by dense seismic observations, *Tectonophysics*, *647*, 63–72, doi:10.1016/j.tecto.2015.02.013.